ISSN 1063-7737, Astronomy Letters, 2018, Vol. 44, No. 2, pp. 67–80. © Pleiades Publishing, Inc., 2018.
Original Russian Text © I.A. Mereminskiy, E.V. Filippova, R.A. Burenin, S.Yu. Sazonov, M.N. Pavlinsky, A.Yu. Tkachenko, I.Yu. Lapshov, A.E. Shtykovskiy, R.A. Krivonos, 2018, published in Pis'ma v Astronomicheskii Zhurnal, 2018, Vol. 44, No. 2, pp. 87–101.

A Deep Extragalactic Survey with the ART-XC Telescope of the Spectrum-RG Observatory: Simulations and Expected Results

I. A. Mereminskiy*, E. V. Filippova, R. A. Burenin, S. Yu. Sazonov, M. N. Pavlinsky, A. Yu. Tkachenko, I. Yu. Lapshov, A. E. Shtykovskiy, and R. A. Krivonos

Space Research Institute, Russian Academy of Sciences, Profsoyuznaya ul. 84/32, Moscow, 117997 Russia

Received July 10, 2017

Abstract—To choose the best strategy for conducting a deep extragalactic survey with the ART-XC X-ray telescope onboard the Spectrum–Röntgen–Gamma (SRG) observatory and to estimate the expected results, we have simulated the observations of a $1.1^\circ \times 1.1^\circ$ field in the 5–11 and 8–24 keV energy bands. For this purpose, we have constructed a model of the active galactic nuclei (AGN) population that reflects the properties of the X-ray emission from such objects. The photons that "arrived" from these sources were passed through a numerical model of the telescope, while the resulting data were processed with the standard ART-XC data processing pipeline. We show that several hundred AGNs at redshifts up to $z \approx 3$ will be detected in such a survey over 1.2 Ms of observations with the expected charged particle background levels. Among them there will be heavily obscured AGNs, which will allow a more accurate estimate of the fraction of such objects in the total population to be made. Source confusion is expected at fluxes below 2×10^{-14} erg s^{-1} cm^{-2} (5–11 keV). Since this value can exceed the source detection threshold in a deep survey at low particle background levels, it may turn out to be more interesting to conduct a survey of larger area (several square degrees) but smaller depth, obtaining a sample of approximately four hundred bright AGNs as a result.

DOI: 10.1134/S1063773718020044

Keywords: *sky surveys, X-ray sources, active galactic nuclei.*

INTRODUCTION

The astrophysical Spectrum–Röntgen–Gamma (SRG) observatory is scheduled to be launched in 2018. Two X-ray instruments will operate onboard SRG: the eROSITA telescope (Predehl et al. 2010; Merloni et al. 2012) sensitive in the soft X-ray 0.2–10 keV energy band and the ART-XC telescope (Pavlinsky et al. 2011, 2016) designed for observations in a harder band, from 5 to 30 keV. The first four years of SRG operation will be devoted to an all-sky survey in the mode of scanning observations, whereupon the observations of individual sources and sky fields are planned to be performed.

One of the main tasks of the ART-XC telescope is to study the population of active galactic nuclei (AGNs) in a hard X-ray band at energies ~10 keV or higher. The gas–dust torus surrounding the central supermassive black holes (SMBHs, Krolik and Begelman 1988) in galactic nuclei can partially or completely obscure the X-ray emission generated in the immediate vicinity of the SMBH, depending on the direction to the observer. In this case, the soft X-ray emission turns out to be suppressed by several orders of magnitude. The harder X-ray emission is less absorbed and, moreover, can be enhanced through Compton scattering (Sazonov et al. 2015). Thus, hard X-ray observations turn out to be necessary to obtain an AGN sample less biased by selection effects.

During the flight of the SRG observatory to the Lagrange point L2, it is planned to perform a deep survey of a small sky field, ~1 deg^2, with a total exposure time of ~1 Ms in order to obtain a homogeneous and complete AGN sample. Similar fields were previously observed both in the standard X-ray band (0.5–10 keV) with the Chandra (Giacconi et al. 2002; Murray et al. 2005) and XMM-Newton (Hasinger et al. 2007) telescopes and in the harder 8–24 keV energy band with the NuSTAR telescope (Alexander et al. 2013). This allowed 93 and 35% of the cosmic X-ray background (CXB) to be resolved into individual sources in the 2–7 (Luo et al. 2017) and 8–24 keV (Harrison et al. 2016) X-ray bands, respectively.

To conduct such surveys, it is necessary to properly choose the survey area-to-depth ratio: a survey

*E-mail: i.a.mereminskiy@gmail.com

of large area and small depth may not give a sufficient sample of distant and faint objects, while an excessively deep survey will run into the source confusion, which will not allow the sensitivity to be increased by increasing the exposure time. In addition, the charged particle background that also reduces the telescope sensitivity should be taken into account.

The goal of this paper is to test the chosen strategy of extragalactic field observations and to determine its expected results, including those for various charged particle background levels. For this purpose, we have simulated the ART-XC observations of a small sky field populated exclusively by AGNs. Below we describe the ART-XC telescope, present the procedure for constructing a model of the AGN population, describe the simulations of observations and simulated data processing, and discuss the properties of the sample of AGNs detected in these observations.

THE ART-XC TELESCOPE

The ART-XC telescope (Pavlinsky et al. 2011, 2016) consists of seven identical co-aligned modules operating in the 5–30 keV energy band. Each module has its own mirror system of 28 nickel–cobalt grazing-incidence mirrors (of Wolter-I type, with iridium coating) and a cadmium–tellurium double-sided strip detector. The typical angular diameter containing half of the focused photons is $27''-34''$ on the telescope axis at energy 8 keV (Krivonos et al. 2017) for different modules, while the effective area of each module is 65 cm^2 at 8 keV. The field of view for each module is about $36'$ in diameter. The shape of the point spread function (PSF) is approximately the same in the central part of the field of view $18'$ in diameter.

The photodetectors (X-ray detectors, Levin et al. 2014, 2016) are $30 \times 30 \times 1$ mm CdTe crystals with 520-μm-wide conductor strips deposited on two sides; the strip spacing is 75 μm. The strip angular size is determined by the focal length (2700 mm) and is about $45''$. The strips (48 on each side) on different photodetector sides are oriented perpendicularly, which allows the recorded photon coordinates to be determined. The dead time of the photodetector is 0.77 ms, and the energy resolution is $\leq$1.2 keV at energy 14 keV.

The photodetector is covered by a housing with a beryllium entrance window 30 mm in diameter; the beryllium thickness is 100 μm. The housing is made of an aluminum–magnesium alloy plated with copper and tin layers 1 mm in thickness each. Since the beryllium window size is slightly smaller than the detector size, the corners of the photodetector array are not exposed to the X-ray photons focused by the mirrors. This allows the charged particle background level to be estimated directly during the observations. A retractable $^{55}Fe + {}^{241}Am$ calibration source is envisaged for the detector energy calibration.

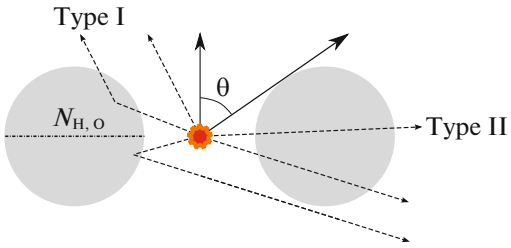

Fig. 1. (Color online) Geometry of the gas–dust torus around the SMBH: θ is the torus half-opening angle and $N_{H,0}$ is the column density on the torus equator.

The telescope turns out to be most efficient in the $\sim$5–11 keV band when a sky survey is conducted, because the effective area of the mirror system decreases sharply at energies above 11.215 keV (Gubarev et al. 2014)—this energy corresponds to the L_3 $2p_{3/2}$ shell of iridium; furthermore, the effective area rapidly decreases with increasing distance from the optical axis at higher energies. In the mode of pointed observations the sources close to the center of the ART-XC field of view can be observed in a harder energy band, approximately up to 30 keV.

THE CATALOG OF SOURCES FOR SIMULATIONS

To simulate a deep extragalactic ART-XC survey, it is first necessary to produce a catalog of AGNs that will be observed. Such a catalog must reproduce the properties of the populations observed in surveys performed in energy bands close to the ART-XC band, such as XMM-Cosmos (Cappelluti et al. 2009), the XMM-Newton Hard Bright Serendipitous Sample (HBSS) (Della Ceca et al. 2004), and the NuSTAR extragalactic surveys (Harrison et al. 2016). In addition, the combined emission from the simulated sources must have a spectrum close to the hard X-ray background spectrum (Revnivtsev et al. 2003; Churazov et al. 2007; Ajello et al. 2008).

The ART-XC field of view is $36'$ in diameter, but photons from sources located up to $50'$ from the optical axis can reach the photodetector via single reflections from the mirrors. Consequently, to take into account the possible effects of detector exposure to photons from sources outside the field of view when simulating the observations of a field with sizes of about $1^\circ \times 1^\circ$, it turned out to be necessary to populate a field of larger sizes, $3^\circ \times 3^\circ$, by sources.

The AGN Population Model

A gas–dust torus that can both obscure and partially reflect the emission from the central SMBH, depending on the angle between its axis and the direction to the observer, is known to be present in many (if not all) AGNs (see Fig. 1). Thus, AGNs are naturally divided into two types: unobscured (type 1) and obscured (type 2). In the case of unobscured AGNs, the emission from the central source is observed both directly and through its reflection from the torus (as a result, the so-called "Compton hump" is observed in the X-ray spectra of AGNs). Hereafter, all objects with a measured absorption column density on the line of sight $N_H < 10^{22}$ cm^{-2} will be labeled as unobscured. Obscured AGNs can be Compton-thin, $N_H = 10^{22}$–10^{24} cm^{-2}, or Compton-thick, $N_H > 10^{24}$ cm^{-2}, depending on what optical depth is accumulated on the observer's line of sight. The contribution of the component associated with the reflection of emission from the torus to the X-ray spectra of obscured AGNs can be very significant.

To produce the sought-for catalog of sources, we used a model of the AGN population based on the following assumptions:

(1) The AGN space density depends in a certain way on the intrinsic X-ray luminosity of the AGN central source (SMBH) and redshift.

(2) Each AGN consists of a geometrically small region in which X-ray emission is generated and a torus of cold matter surrounding it. The AGN central source radiates isotropically, while its spectrum is described by a power law with an exponential cutoff.

(3) The half-opening angle of the torus is a function of the intrinsic X-ray luminosity of the AGN central source and redshift, while the torus surface density in the equatorial plane varies from object to object in some (wide) range.

Each of these assumptions is discussed in more detail below in the corresponding sections. Everywhere below we use the standard cosmological parameters: $\Omega_m = 0.3$, $\Omega_\Lambda = 0.7$, and $H_0 = 70$ km s^{-1} Mpc^{-1}.

The AGN Luminosity Function

Measuring the dependence of the AGN space density on the X-ray luminosity of the central SMBH, i.e., the X-ray luminosity function (XLF) of AGNs, is a complex task that requires simultaneously taking into account a large amount of heterogeneous observational data. We used the XLF derived by Ueda et al. (2014) (hereafter U14) based on samples of AGNs from the surveys conducted with the ASCA, Swift/BAT, Chandra, XMM-Newton, and ROSAT telescopes. At redshift $z = 0$ it is described by two power laws:

$$\frac{d\Phi_X(L_X)}{d\log L_X} A\left[\left(\frac{L_X}{L_*}\right)^{\gamma_1} + \left(\frac{L_X}{L_*}\right)^{\gamma_2}\right]^{-1}, \quad (1)$$

where L_X is the intrinsic rest-frame X-ray 2–10 keV luminosity of the AGN, $A = 2.91 \times 10^{-6} h_{70}^3$ Mpc^{-3}, $L_* = 10^{43.97} h_{70}^{-1}$ erg s^{-1}, $\gamma_1 = 0.96$, and $\gamma_2 = 2.71$. The XLF at nonzero z is found by additionally multiplying the dependence (1) by an evolution factor $e(L_X, z)$ dependent on the intrinsic luminosity and redshift (see U14). The XLF evolution with z is shown in Fig. 2. The U14 model is applicable for describing the XLF evolution up to $z = 6$.

The Torus Opening Angle and Column Density

The contribution of Compton-thick AGNs is disregarded in the dependence (1). Ueda et al. (2014) also introduced a function $\Psi(L_x, z)$, the ratio of the number of Compton-thin ($\log N_H = 22$–24) obscured AGNs to the total number of unobscured ($\log N_H < 22$) and Compton-thin obscured AGNs, and, in addition, estimated the ratio of the number of Compton-thick AGNs to the number of Compton-thin obscured AGNs: $f \approx 1$. Thus, the total number of AGNs, including the Compton-thick ones, in a chosen sky field can be found as

$$N = \Omega_s \int_0^6 \int_{40}^{47} \frac{d\Phi_X(L_X, 0)}{d\log L_X} e(L_x, z) \quad (2)$$
$$\times (1 + f\Psi(L_X, z)) \frac{dV}{dz} dz d\log L_X,$$

where dV is a comoving volume element of the Universe, and Ω_s is the ratio of the survey area to the total sky area.

In our model the observed fraction of obscured objects is assumed to be directly related to the half-opening angle of the torus θ (see Fig. 1) in an AGN of fixed luminosity L_x at fixed redshift z. In accordance with the above definitions, the number of unobscured AGNs is proportional to $1 - \Psi$, while the number of obscured (including Compton-thick) AGNs is proportional to $(1 + f)\Psi \approx 2\Psi$. Thus, we find that

$$\cos\theta = \frac{(1+f)\Psi}{1 - \Psi + (1+f)\Psi} \approx \frac{2\Psi}{1+\Psi} \quad (3)$$

and, consequently,

$$\cos\theta(L_x, z) \approx \frac{2\Psi(L_x, z)}{1 + \Psi(L_x, z)}. \quad (4)$$

Next, it is assumed in our model that the torus column density in the equatorial plane $N_{H,0}$ for fixed

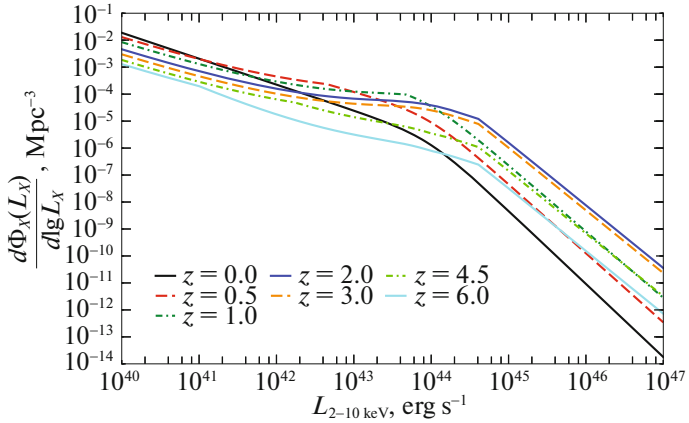

Fig. 2. (Color online) Evolution of the X-ray luminosity function for AGNs (without Compton-thick objects) with redshift according to the Ueda et al. (2014) model.

L_x and z can take various values. It was shown in U14 that the distribution of $\log N_H$ in AGNs is approximately flat in a wide range, from 22 to 26. A similar result was obtained by Sazonov et al. (2015) based on a sample of AGNs from the INTEGRAL hard X-ray sky survey. In this case, it should be kept in mind that our model (see Fig. 1) differs significantly in geometry from the Brightman and Nandra (2011) model used in U14, in which the cold matter is located not in the torus but in a sphere with two conical openings. The column density of matter on the line of sight in this model is equal to the equatorial one for all viewing angles $\alpha > \theta$ and zero for $\alpha < \theta$. In contrast, in our model the column density of matter on the line of sight depends on the viewing angle as follows:

$$N_H(\alpha) = N_{H,0}\sqrt{1 - \left(\frac{\cos\alpha}{\cos\theta}\right)^2} \qquad (5)$$

and, hence, the column density averaged over the "obscured" directions is $\langle N_H\rangle = (\pi/4)N_{H,0}$. Therefore, to approximately compensate for this difference in geometry, we shifted the range of admissible equatorial column densities for the torus from $\log N_{H,0} = 22{-}26$, as in U14, to $\log N_{H,0} = 22.3{-}26.3$.

Template AGN Spectra

The X-ray spectra of AGNs can include several components: the direct emission from the central source, the emission reprocessed by the gas–dust torus, the emission reflected from the accretion disk (both these components contribute to the formation of a strong fluorescent iron line at energy 6.4 keV), and the so-called "soft excess" at energies below 1 keV whose nature is not yet clear. Since the soft excess dominates at energies outside the ART-XC working range, it was disregarded in our model.

To take into account the effects of emission reprocessing by the torus, we used Monte Carlo simulations (for a description of the simulation technique, see Churazov et al. 2008) similar to those described in Sazonov et al. (2015). We created a library of templates on a fine grid of torus half-opening angles θ and equatorial column densities $N_{H,0}$ as well as viewing angles α. The spectrum of the central source was assumed to be a power law with an exponential cutoff: $dN/dE \propto E^{-\Gamma}e^{-E/E_{\mathrm{cut}}}$, where $\Gamma = 1.9$ and $E_{\mathrm{cut}} = 300$ keV (typical for both nearby Seyfert galaxies and distant quasars; see, e.g., Dadina 2008; Sazonov et al. 2008). The elemental abundances were assumed to be solar (Feldman 1992).

The component describing the reflection of the emission of the central source from a cold accretion disk, the `pexrav` model in the xspec software (Magdziarz and Zdziarski 1995), was also added to the template spectrum, because such a component was present in the U14 model. The disk rotation axis was assumed to be co-aligned with the torus axis, while the reflectivity was taken to be $R_{\mathrm{refl}} = 0.5$. In those cases where the observer's line of sight crossed the torus, we took into account the photoabsorption (`phabs` in xspec) of the photons reflected from the disk. In addition, to roughly take into account the photoabsorption in the interstellar medium of the host galaxies, we added an absorption of 10^{21} cm^{-2} for all AGNs.

The Algorithm for Constructing the AGN Catalog

Thus, the algorithm for constructing the original catalog of AGNs was as follows. First, from Eq. (2) we calculated the expected number of AGNs $\langle dN\rangle$ in a small comoving volume element of the Universe dV in a range of redshifts from z to $z + dz$ and a small range of luminosities from L_X to $L_X + dL_X$.

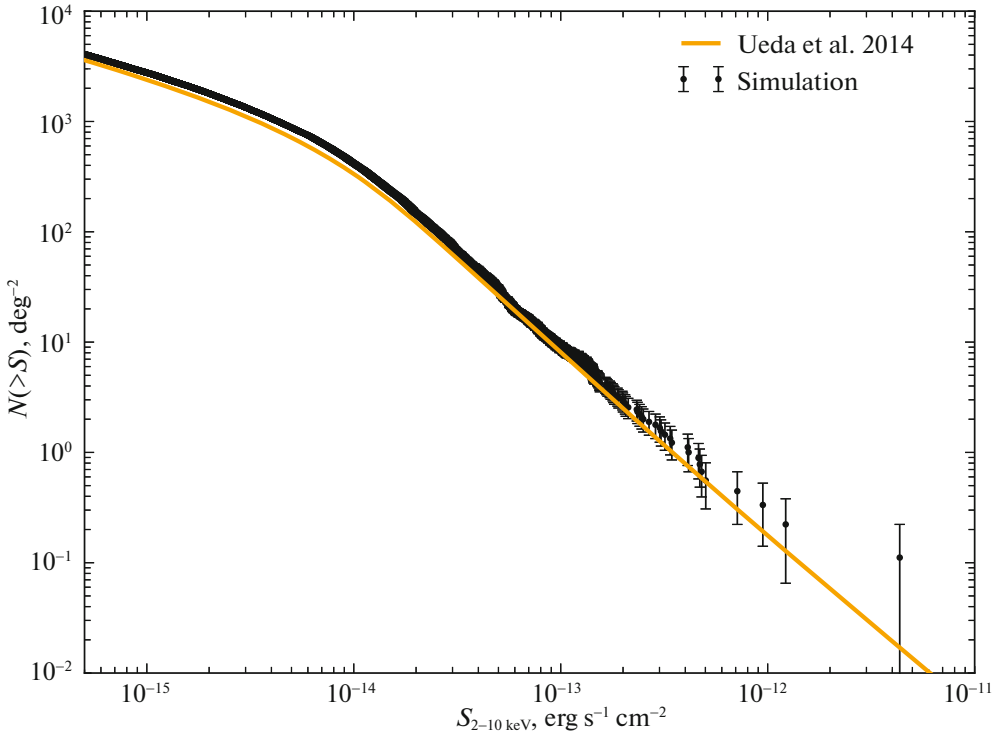

Fig. 3. (Color online) The AGN $\log N - \log S$ relation in the 2–10 keV energy band constructed from our simulations. The orange line indicates the predicted $\log N - \log S$ relation from U14.

The number of AGNs was then determined from the Poisson distribution $dN_{L_X,z} = P(\langle dN \rangle)$. Next, from Eq. (4) we determined the half-opening angle of the torus. Then, the direction to the observer, the celestial coordinates, and $\log N_{H,0}$ (inside the range 22.3–26.3) were randomly drawn for each AGN. Finally, in accordance with the set of parameters found, we selected the X-ray spectrum from the library of templates and calculated the observed X-ray flux for each AGN. We applied the K-correction due to the cosmological redshift.

The Final AGN Catalog

The catalog contains a total of about three million AGNs with luminosities L_X from 10^{40} to 10^{47} erg s^{-1} and redshifts from 0 and 6 populating a field of 9 deg^2. As can be seen from the $\log N - \log S$ relation in Fig. 3, our model corresponds well to the predictions from U14 at fluxes above 10^{-14} erg cm^{-2} s^{-1}, while at lower fluxes it predicts a larger number of sources by 10–20%. This discrepancy is comparable to the residuals between the various count measurements at these fluxes (see, e.g., Cappelluti et al. 2009; Ranalli et al. 2013; etc.).

Since no constraints on the minimum flux were introduced, the total spectrum of AGNs in the field agrees well (see Fig. 4) with the observed spectrum of the cosmic X-ray background. The slight deficit of emission at high energies may stem from the fact that we disregarded the observed scatter of power-law slopes and exponential cutoffs in the spectra of individual AGNs.

To store the produced catalog, we used the *SIMPUT* format,[1] an extension of the *FITS* standard (Wells et al. 1981) designed to work with the input catalogs for the simulations of observations with X-ray telescopes.

SIMULATIONS OF OBSERVATIONS

To produce a list of photons, we used the *SIXTE* package.[2] The photons from all sources in a $3° \times 3°$ field, given the area of the ART-XC entrance aperture 1212.9 cm^2 for all seven X-ray mirror systems (XMSs), were included in the list. The exposure time was 1.2 Ms; the admissible energies for photons were limited by the range 2–50 keV. To take into account the possible effects of detector exposure to photons from sources outside the field of view, we drew the photons from all sources in our field at each instant of time. A total of ~52 million photons were drawn.

[1] http://hea-www.harvard.edu/heasarc/formats/simput-1.1.0.pdf.

[2] http://www.sternwarte.unierlangen.de/research/sixte/index.php.

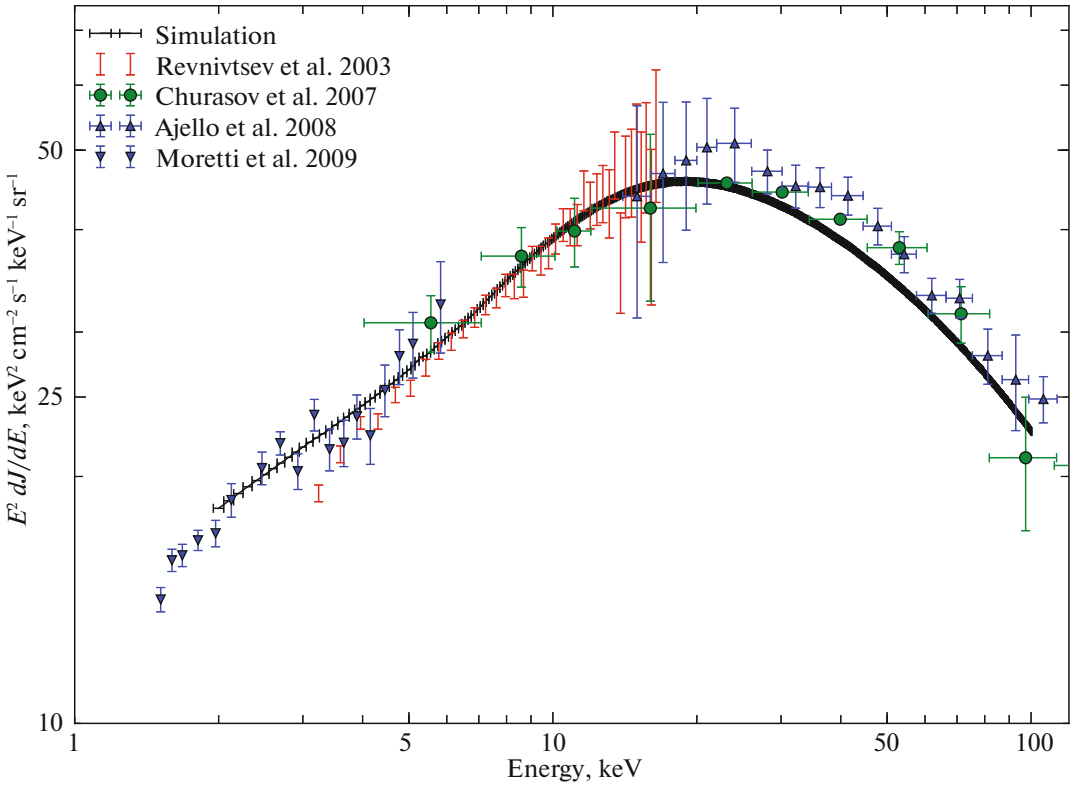

Fig. 4. (Color online) Comparison of the simulated X-ray background spectrum (black) with the experimental data in the following energy ranges: 1.5–7 (Moretti et al. 2009), 3–20 (Revnivtsev et al. 2003), 5–100 (Churazov et al. 2007), and 15–200 keV (Ajello et al. 2008).

To properly estimate the sensitivity of the telescope, it is necessary to take into account the radiation situation near the Lagrange point L2 and the corresponding count rate of events associated with charged particles. The background count rate has been estimated previously for other X-ray telescopes that will operate at L2, eROSITA (Tenzer et al. 2010) and ATHENA (Lotti et al. 2016). Despite the fact that the results obtained in these papers cannot be directly extended to ART-XC due to the differences in geometry, photodetector type, etc., it seems reasonable to assume that the characteristic count rate of background events will not change to within an order of magnitude. For our simulations we chose two values corresponding to low (10^{-3} cm^{-2} s^{-1} keV^{-1}) and high (10^{-2} cm^{-2} s^{-1} keV^{-1}) background levels.

To simulate a deep survey of our field with AGNs, we simulated the scanning of a central $1^\circ \times 1^\circ$ field by the telescope with a $5'$ step. We specified that the telescope should successively perform 169 (13×13) pointings with an exposure of 6950 s each. Between the pointings the telescope axis was moved with a speed of 0.03 deg s^{-1}. In addition, about 150 s before each pointing was allocated for the transition processes. The total scanning duration was about 1.2 Ms. The positions of the telescope axes during the entire observing session were written with a step of 1 s for the subsequent use.

Next, we drew each photon between the seven mirror systems and determined the angles at which the photon fell on the XMSs based on the spatial orientation of the telescope at a given moment of time.

The passage of photons through the mirror system to the detector was calculated by the ray-tracing technique. In our model we used an XMS design fairly close to the actual one from the viewpoint of photon passage. Apart from the mirror shells themselves, we took into account the spider, the central diaphragm, and the inner baffle. The geometry of the mirror shells and their arrangement in the XMS were assumed to be ideal. The reflecting surface of the mirrors is a 10-nm-thick iridium (Ir) layer on a nickel (Ni) substrate with a surface roughness of 1 nm. The reflectivities were calculated from the Fresnel equations that were modified using the Nevot–Croce factor (Nevot and Croce 1980) to take into account the surface roughness. The filters and structures in the path of the emission in the real telescope were added to the model: the mylar filter with a deposited aluminum layer before the XMS, the detector collimator, and the detector housing with a beryllium window. For each photon falling into the detector, based on the system geometry, we calculated the probability

that this photon would reach the detector and would be recorded in it from the mirror reflectivities and the filter transmittivities.

The physical coordinates on the detector, energy, and time were written for the photons recorded in the detector. These values were converted to a binary form corresponding to the telemetry packets of the X-ray detector. For example, the strip number X and Y was calculated from the coordinates on the detector. The event energy was "spread" with the energy resolution and converted to the amplitude using the calibrated energy–amplitude-to-digital converter (ADC) channel values taken from one of the standard X-ray detectors (detector–donor for simulations). The noise pedestal of a given strip determined in the donor calibrations was also added to the amplitude. The charged particle background was also added at this stage. We drew the intervals between background events from a given charged particle count rate and a detector dead time of 0.77 ms and then placed the background events into a general time scale. The charged particle coordinates were drawn uniformly on the detector surface; the energy was specified in accordance with a flat charged particle background spectrum in the range 3–200 keV. Subsequently, the background events were converted to a binary form just as the events passed through the XMS. All of the events (useful and background) were combined into a single list of events, were sorted by time, and were written in the telemetry packets of the X-ray detector.

The X-ray detector service packets needed to process the information were additionally formed. For this purpose, we used the corresponding detector–donor packets in which the detector identifiers and time were replaced. Thus, the software for fast processing and checking the detector state can also be tested based on the set of simulated data.

The previously written data on the telescope pointing were converted to the orientations of the spacecraft star trackers. There will be three such trackers on the spacecraft, each having its own known orientation with respect to the spacecraft axes. The data from all trackers must be transferred to the telescope memory every second. Binary telemetry packets in the formats corresponding to each of the three star trackers were formed from these data.

The telemetry packets of the ART-XC detectors were combined with the packets of the star trackers, were sorted by time, and were written into a file that corresponded to a typical ART-XC data transmission during a spacecraft–Earth communication session. Thus, the data were subsequently processed using the entire ART-XC data processing pipeline.

PROCESSING THE SIMULATION RESULTS

The Standard Data Processing Pipeline

The telemetry packets were processed using a preliminary version of the standard ART-XC data processing pipeline. The pipeline software is designed to obtain clean calibrated lists of events and accompanying telemetry information. This software is currently being developed at the Space Research Institute of the Russian Academy of Sciences. The simulated data that are discussed in this paper were used to fine-tune this software

The data are processed in three main steps: raw data conversion (level 0), calibration (level 1), and filtering (level 2). Each of these levels is realized by a set of independent software modules developed to be used jointly with the FTOOLS/HEASOFT X-ray data processing package.

At level 0 the data streams from the X-ray telescopes, the pointing and telemetry data are separated, whereupon these data are converted to the FITS format. At level 1 the photon list is calibrated, which includes the determination of event multiplicity (i.e., the number of strips in which the energy release exceeded some threshold; only the events with multiplicity 1, 2, or 3 are used), the amplitude reconstruction, and the conversion of event amplitudes to energies. Good time intervals (GTI) are formed on the basis of the incoming data and information about the instrument operation conditions. In addition, the observatory pointing data are calculated and the celestial coordinates of the photon arrival are reconstructed at this level. At level 2 the photons are filtered in accordance with the formed good time intervals, including the user good time intervals if they will be provided. The parameters of the observation time and the mean count rate are calculated and the observation start and end times are determined for the produced clean photon list.

The cleaned, calibrated lists of events and the pointing files are the result of the standard data processing pipeline operation (level 2).

Constructing Sky Maps and Source Detection

Using the calibrated lists of events and the telescope pointing data, we constructed X-ray images of the sky, exposure and background maps. The software designed for this purpose was also included into the standard telescope software package (level 3) that is currently being developed at the Space Research Institute of the Russian Academy of Sciences.

It is well known that the most sensitive method for source detection is optimal filtering, i.e., a convolution of the image with the function reflecting the expected source signal shape. The point spread function

(PSF) for the ART-XC mirrors was carefully calibrated at the Marshall Space Flight Center (Krivonos et al. 2017) and the Space Research Institute of the Russian Academy of Sciences. However, the ART-XC telescope is peculiar in that the characteristic size of the weighted mean PSF for the mirrors turns out to be comparable to the image pixel size on the photodetector. The effective PSF in this case is a convolution of the PSF for the mirrors with a square window of a size equal to the image pixel size on the photodetector, which is similar in its shape to such a square window.

On this basis, we used the photon images convolved with a square window of a size equal to the photodetector image pixel size in searching for sources. Since the total image had a much finer partitioning compared to the photodetector image pixel size, information about the most probable position of each photon, given the spacecraft pointing data and the photodetector shift in the focal planes of each of the seven telescope modules that were calibrated based on the simulated observational data for bright sources, was retained in it.

Strictly speaking, the image obtained in this way would be optimally filtered only if the size of the PSF for the mirrors were much smaller than the photodetector pixel size. Since this condition is not fulfilled completely in our case, the image construction method described above was used as a first approximation. Later on, we are going to develop a procedure of searching for sources by taking into account the precise PSF shape. This must increase the sensitivity of the source detection in the ART-XC data.

We constructed the exposure map based on the vignetting maps that were calculated by the ray-tracing technique on a photon energy grid. These maps were averaged in a given energy range with a weight proportional to the photon spectrum with a photon index of -1.7, which roughly corresponds to the averaged AGN spectrum. The photodetector efficiency was assumed to be constant over the field within an entrance window 30 mm ($39'$) in diameter. The photon detection efficiency map constructed in this way was extended to the sky by taking into account the telescope pointing data and the photodetector shift in the focal plane; the efficiency of all seven telescope modules was assumed to be the same.

The time-varying particle background was estimated from the unexposed photodetector regions located at the array corners outside the entrance window. Based on these data and using also the telescope pointing data, we also constructed the particle background map.

The cosmic X-ray background (CXB), i.e., the total emission of the faint, unresolved AGNs from the original catalog, accounts for a significant fraction of the background recorded on the photodetector. This background component cannot be modeled by a quantity proportional to the exposure time, because the relatively few and bright sources with fluxes that are not much lower than the detection threshold contribute significantly to the background. As a result, the CXB turns out to be variable over the field, and it should be measured from the observational data. For this purpose, all of the small-scale structures with a size less than $\approx 5'$ were removed in the image using a wavelet decomposition (Vikhlinin et al. 1998); the remaining image was used as the background.

In our search for sources the energy range was limited to 5–11 keV. The source detection threshold was chosen to be 4.5σ. After the initial tests, it emerged that the measured fluxes from bright sources systematically exceeded the true ones approximately by 15%, possibly because the average AGN spectrum used to calculate the fluxes was inaccurate. This question will be investigated in detail in future; for the simple estimates that are the goal of our paper it will suffice to introduce an appropriate correction factor.

The size of the field in which the search for sources was conducted was limited to $1.1^\circ \times 1.1^\circ$, with the effective exposure time at the field edges being approximately half of the maximum one (50 and 110 ks, respectively). Figure 5 shows the X-ray images of the sky obtained by the method described above for two particle background levels. The image quality (PSF) in the survey was about $60''$ (the full width at half maximum). It is clearly seen that an increase in the background causes the number of detected sources to decrease and the noise to increase in the central part of the image. Figure 5 also shows the 8–24-keV sky image at a low background level.

PROPERTIES OF THE PRODUCED AGN SAMPLE

The method used revealed 394 sources with fluxes (5–11 keV) above 7×10^{-15} erg s^{-1} cm^{-2} in the case of a low background (10^{-3} cm^{-2} s^{-1} keV^{-1}). In the case of a high background (10^{-2} cm^{-2} s^{-1} keV^{-1}), we managed to detect 179 sources with fluxes above 1.5×10^{-14} erg cm^{-2} s^{-1}, i.e., the detection threshold approximately doubled as the background rose by an order of magnitude. The median deviation of the positions of the detected sources (without the false ones, see below) from the true positions of their counterparts from the original catalog was $10.0''$ and $10.5''$ in the case of a low and high background, respectively. The localization accuracy for bright sources with fluxes above 5×10^{-14} erg cm^{-2} s^{-1} is considerably better, about $6.5''$, irrespective of the background level.

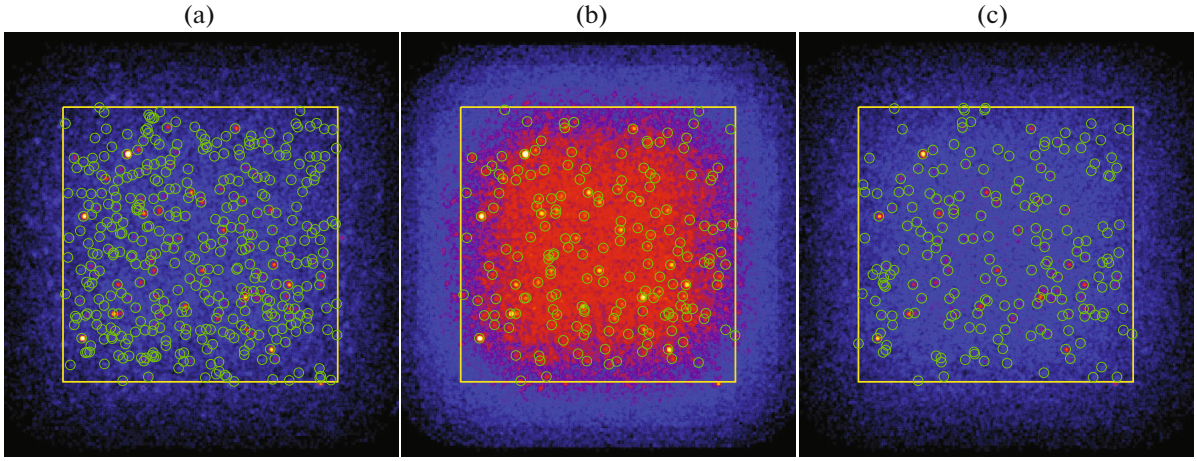

Fig. 5. (Color online) ART-XC X-ray images of the sky from the simulated data. (a) in the 5–11 keV band in the case of a low particle background (10^{-3} counts cm^2 s^{-1} keV^{-1}), (b) in the same band but with a high background (10^{-2} counts cm^2 s^{-1} keV^{-1}), and (c) in the 8–24 keV band with a low background level. The yellow square indicates the central part of the field ($1.1^\circ \times 1.1^\circ$) in which the search for sources was conducted. The green circles mark the detected sources.

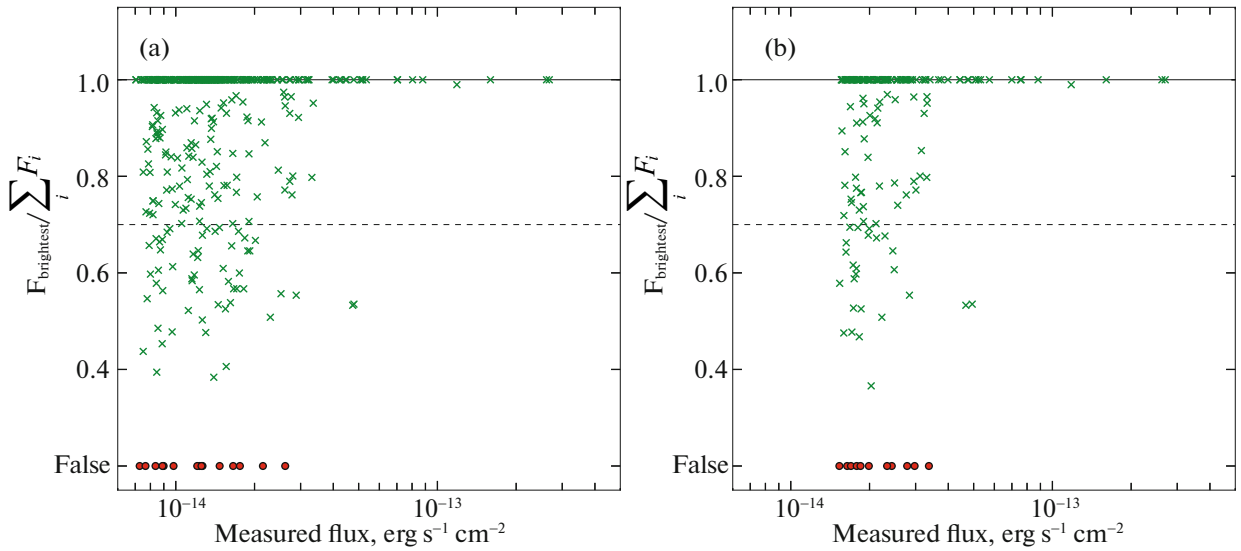

Fig. 6. (Color online) Dependence of the contribution of the brightest source to the total flux from all sources from the original catalog in the identification circle on the measured flux from the detected source; (a) for the case of a low particle background: a total of 394 sources were detected, among them 15 are false and 54 are confused; (b) for the case of a high background: a total of 179 sources were detected, among them 11 are false and 25 are confused. The red dots mark the false sources. The dashed line indicates the adopted admissible confusion level.

At the lowest recorded fluxes the surface density of sources reaches ~400 per deg^2, while the characteristic distances between sources are close to the angular resolution of the telescope. Under such conditions faint sources can begin to mix, i.e., one source with a flux equal to the sum of the fluxes from faint sources will be detected instead of two or more sources with low fluxes. It can roughly be assumed that the confusion begins to have an effect when the density of sources reaches one object per 30–40 characteristic areas of the telescope PSF whose effective size (diameter) is about 60″. Hence it follows that the mixing limit must be reached at a density of ~100 sources per deg^2, corresponding to a 5–11 keV flux $\sim 1.5 \times 10^{-14}$ erg s^{-1} cm^{-2}, which is well above the source detection threshold in the case of a low

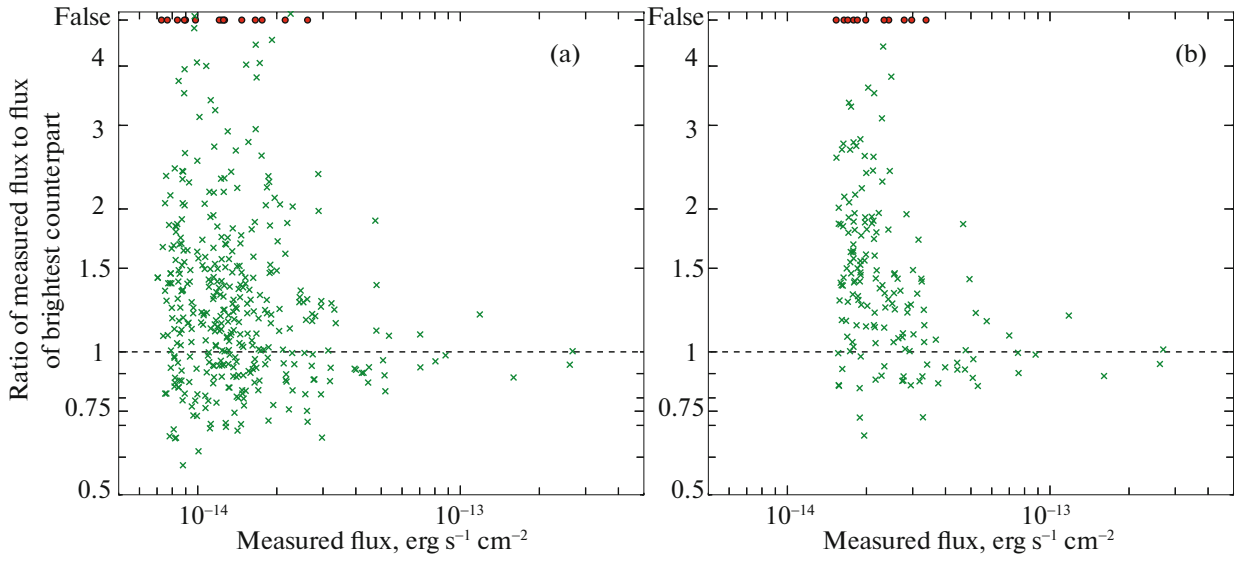

Fig. 7. (Color online) Relation between the measured flux of the detected source and the flux of the brightest counterpart from the original catalog; (a) for the case of a low particle background, (b) for the case of a high background. The red dots mark the false sources.

background. Apart from confused sources, obviously, false sources must also be encountered in our sample.

The knowledge of the catalog of original sources allows us to find the mixed and false sources in the sample. For each detected source we determined the identification circle in which its counterpart from the original catalog was searched for. For sources with a significance less than 5σ the circle radius was taken to be $30''$; for more significant sources the radius was linearly reduced to $20''$ at a 6σ significance and subsequently remained constant. The size of the identification circle we chose ($20''-30''$ in radius) is close to the observed full width at half maximum of the effective telescope PSF ($30''$). Then, we searched for the brightest source in the original catalog. If no such counterpart was found among the bright sources of the catalog (with a 5–11 keV flux above 10^{-15} erg s^{-1} cm^{-2}), then the detected source was deemed false. Otherwise, we calculated the total sum of the fluxes from all of the sources falling into the identification circle, and if the contribution of the brightest source to the total flux was less than 0.7, then the source was deemed confused.

In Fig. 6 the ratio of the flux from the brightest counterpart to the total flux from all sources from the original catalog in the identification circle is plotted against the measured flux from the detected sources. In the case of a low background at fluxes below 10^{-14} erg s^{-1} cm^{-2}, we detected 113 sources, among which 6 (5%) are false and 18 (16%) are confused; at fluxes $(1-2)\times10^{-14}$ erg s^{-1} cm^{-2} there are 211 sources, among which 7 (3%) are false and 30 (14%) are confused; at fluxes $(2-4)\times10^{-14}$ erg s^{-1} cm^{-2} there are 50 sources, among which 2 (4%) are false and 4 (8%) are confused; and at higher fluxes, i.e., above 4×10^{-14} erg s^{-1} cm^{-2} there are 20 sources, among which 2 (10%) are mixed and none is confused. In the case of a high background, at fluxes $(1.5-2)\times10^{-14}$ erg s^{-1} cm^{-2}, we detected 80 sources, among which 6 (8%) are false and 16 (20%) are confused; at fluxes $(2-4)\times10^{-14}$ erg s^{-1} cm^{-2} there are 80 sources, among which 5 (6%) are false and 7 (9%) are confused; and, finally, at fluxes above 4×10^{-14} erg s^{-1} cm^{-2} we detected 19 sources, among which 2 (10%) are confused and none is false. Thus, the fractions of false and confused sources decrease with increasing flux, as might be expected.

Figure 7 shows the relation between the measured fluxes from the detected sources and their brightest counterparts: (a) for the case of a low background and (b) for the case of a high background. Note that near the detection threshold the measured flux from the sources is, on average, greatly overestimated relative to the true one not only due to the merging of sources but also due to the so-called Eddington bias (see, e.g., Vikhlinin et al. 1995; Burenin et al. 2007).

Knowing the original catalog allows us to determine the fraction of detected sources as a function of their flux for different background levels and different exposure times. About half of all AGNs at fluxes $\sim10^{-14}$ erg cm^{-2} s^{-1} can be detected at a low background and full exposure (corresponding to the total survey time of 1.2 Ms) (see Fig. 8). Reducing

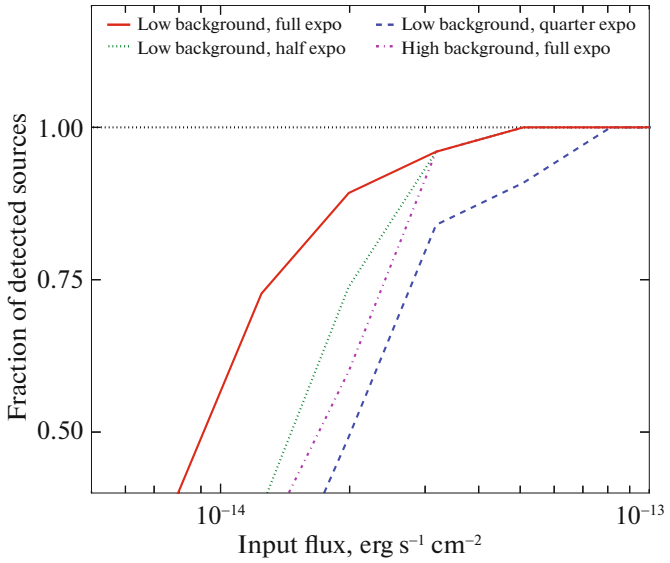

Fig. 8. (Color online) Fraction of detected (in the 5–11 keV band) sources from the original catalog versus their true flux: in the case of a low background and full exposure (red solid line), in the case of a low background and half exposure (green dotted line), in the case of a low background and quarter exposure (blue dashed line), and in the case of a high background and full exposure (purple dash–dotted line).

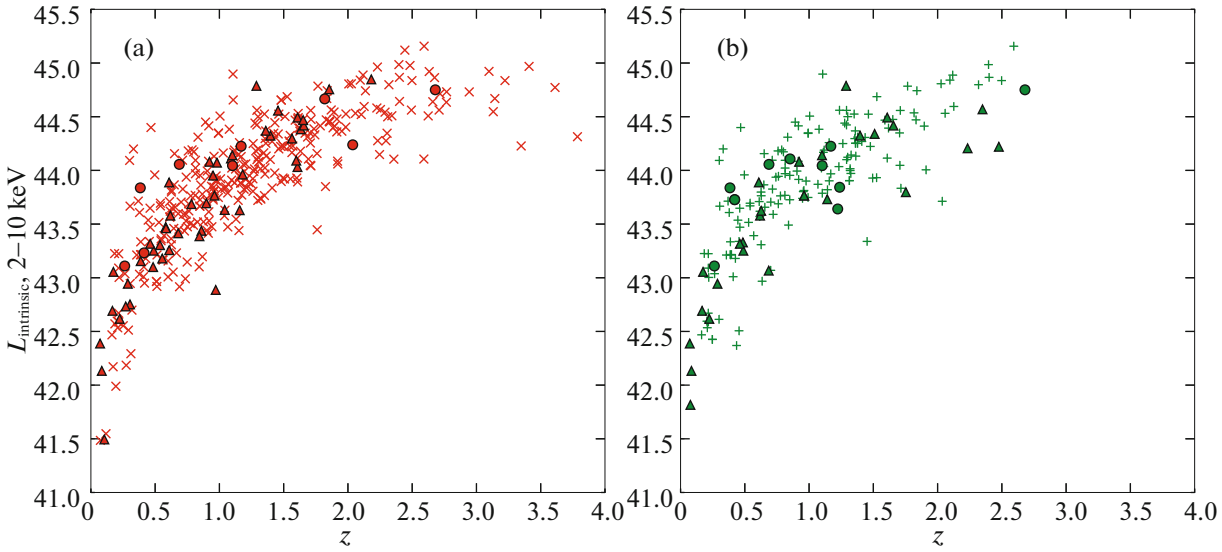

Fig. 9. (Color online) The distribution of detected AGNs in intrinsic X-ray luminosity and redshift for the case of a low background: (a) for the 5–11 keV survey and (b) for the 8–24 keV survey. The squares and circles indicate, respectively, the AGNs with $\log N_H = 23$–24 and Compton-thick AGNs.

the exposure time by half leads to a degradation of the sensitivity to 1.3×10^{-14} erg cm^{-2} s^{-1}; in this case, 202 sources, 4 of which are false, turn out to be detected. At a quarter of the exposure time the sensitivity and the total number of sources turn out to be 1.8×10^{-14} erg cm^{-2} s^{-1} and 118 (3 false), respectively. If only the sources with fluxes above 2×10^{-14} erg s^{-1} cm^{-2}, at which the source mixing effect is comparatively weak (see above), are considered, then it turns out that almost the same number of sources as that in the survey with a full exposure can be detected in the survey with half the exposure. Thus, to increase the size of the high-quality sample of bright AGNs at a given total survey time, it seems

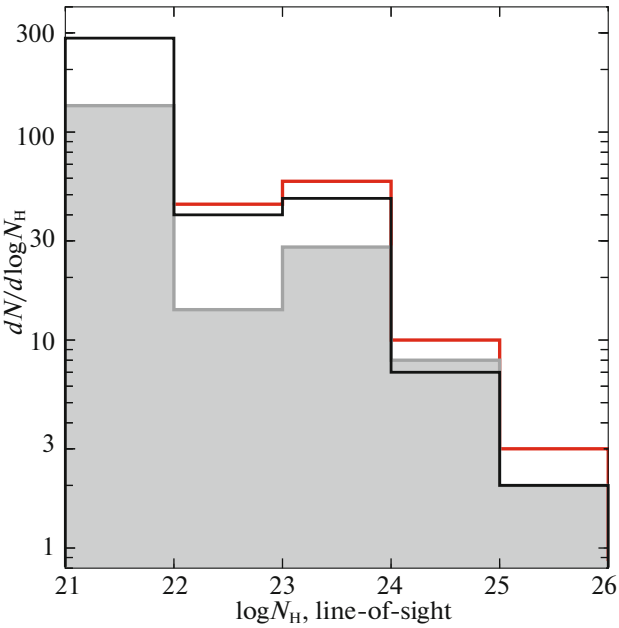

Fig. 10. (Color online) The distribution of detected AGNs in column density on the line of sight for the case of a low background. The black line corresponds to the 5–11 keV survey, the gray histogram corresponds to the 8–24 keV survey. The red color indicates the total number of obscured objects that can be detected by combining the surveys in both bands. The objects with $\log N_H < 22$ may be deemed unobscured.

reasonable to reduce the effective exposure time while increasing the survey area.

The median redshift of the detected AGNs (without any false sources) turned out to be $z \approx 1$ in the cases of a low and high background. The most distant object in the sample with a low background and the sample with a high background turned out to be located at $z = 3.8$ and 3.2, respectively. Heavily obscured AGNs with a column density on the line of sight $\log N_H \geq 23$ are present in both samples: 57 (including 9 Compton-thick AGNs with $\log N_H \geq 24$) and 20 (including 3 Compton-thick AGNs) objects, respectively.

The possibility of using a harder energy band, 8–24 keV, for the detection of sources in the ART-XC survey was considered separately. This band was chosen to coincide with that of the NuSTAR extragalactic surveys (Harrison et al. 2016). In this case, at a low background level the sensitivity was found to be 2.5×10^{-14} erg s^{-1} cm^{-2}, while the total number of detected sources (see the right image in Fig. 5) was 198 (11 false and 25 mixed). The number of heavily obscured AGNs in this sample is 39, among which 10 are Compton-thick.

Most of the AGNs detected in the 8–24 keV band were also detected in the 5–11 keV band. Figure 9 shows the distribution of detected AGNs in intrinsic X-ray luminosity and redshift for both energy bands. As might be expected, the 5–11 keV survey provides a larger sample of AGNs, including those with lower luminosities. However, the survey in the hard X-ray band is of considerable interest from the viewpoint of the detection of heavily obscured AGNs. For example, 4 of the 10 Compton-thick AGNs detected in it are not present in the 5–11 keV sample. Consequently, the total number of such objects detected from the set of data obtained (simultaneously) in the 5–11 and 8–24 keV bands is 13, i.e., larger than the number of Compton-thick AGNs (9) detected only in the 5–11 keV band by one and a half times.

Figure 10 shows the distribution of line-of-sight column densities for the detected objects the black line for the 5–11 keV sample with a low background and the gray filled chart for the sample in the hard X-ray 8–24 keV band. It is important to note the presence of two objects with an absorption column density of more than 10^{25} cm^{-2}. The fraction of obscured ($\log N_H > 22$) AGNs in both samples is about 25%.

CONCLUSIONS

In this paper we completely simulated the observations of an extragalactic field with the ART-XC telescope onboard the SRG observatory, from the production of a synthetic AGN population to the "observation" of photons using a numerical model of the ART-XC telescope and the source detection in the simulated sky images.

The AGN population obtained under simple assumptions showed good agreement with the theoretical predictions and observational data, in particular, we managed to well reproduce the cosmic X-ray background (CXB) spectrum. Owing to our calculations of the passage of photons through the telescope mirror system and the use of the photodetector characteristics determined during our experimental work with the prototype, it became possible to estimate the telescope sensitivity at different expected charged particle background levels. Using a standard telemetry format in packing the simulation data allowed us to check whether the standard data processing pipeline operated properly and to develop a preliminary version of the algorithm of source detection in the ART-XC images.

Our simulations show that it will be possible to obtain an AGN sample consisting of ~400 objects with 5–11 keV fluxes above 7×10^{-15} erg s^{-1} cm^{-2} with the ART-XC telescope for the strategy of a deep survey considered, the examination of a $1.1^\circ \times 1.1^\circ$ field with an effective exposure time of ~100 ks (which is achieved at a total survey time of 1.2 Ms)

and a low particle background level (10^{-3} counts $\times$ cm^2 s^{-1} keV^{-1}). Under less favorable background conditions (10^{-2} counts cm^2 s^{-1} keV^{-1}), one might expect to obtain a sample consisting of $\sim$200 AGNs with fluxes above 1.5×10^{-14} erg s^{-1} cm^{-2}. Such a survey would be quite comparable to the best present-day surveys being conducted at approximately the same energies, such as the COSMOS survey of the XMM-Newton observatory where 1.9 deg^2 were covered in a total observing time of $\sim$1.5 Ms with a sensitivity better than 1.3×10^{-14} erg cm^{-2} s^{-1} in the 5–10 keV energy band (Cappelluti et al. 2009).

However, due to the insufficiently good angular resolution of ART-XC (the FWHM of the effective PSF in the survey is 60″) and the high density of faint AGNs constituting the CXB in the sky, the source confusion effect becomes significant already at fluxes $\sim 2 \times 10^{-14}$ erg s^{-1} cm^{-2}. This makes it difficult to use the subsample of fainter AGNs that can be detected in a deep ART-XC survey for scientific purposes. Therefore, conducting a survey with a smaller depth ($\sim 2 \times 10^{-14}$ erg s^{-1} cm^{-2} in the 5–11 keV energy band) roughly corresponding to the expected effective source confusion threshold, but with a considerably larger area would possibly be a more optimal use of the ART-XC observing time during the SRG flight to the Lagrange point L2. Thus, if the total survey time of 1.2 Ms (about two weeks of observations) is retained, then it will be possible to cover about 3 deg^2 in the sky and to detect $\sim$400 AGNs at a low background level. The ultimate choice of a strategy for observations will depend on the background level that will be measured by the telescope before the survey.

An important distinctive feature of the ART-XC telescope is that it has a significant sensitivity even at energies above 11 keV. As has been shown in this paper, using the harder 8–24 keV energy band in addition to the 5–11 keV band, one can detect an appreciably larger (approximately by one and a half times) number of Compton-thick AGNs that still remain a poorly studied class of objects (especially outside the local Universe) and, therefore, are of particularly big interest. Obviously, combining two or more energy bands must allow a maximum number of AGNs with a different degree of absorption to be detected. We are going to perform such an optimization of the algorithm for the detection of sources with the ART-XC telescope.

In the 8–24 keV energy band the sensitivity of the simulated ART-XC survey with an area of $1.1^\circ \times 1.1^\circ$ turned out to be 2.5×10^{-14} erg s^{-1} cm^{-2}. This is comparable to the sensitivity of the NuSTAR telescope, so far the only grazing-incidence telescope operating in the hard X-ray band, achieved by it in special deep small-area extragalactic surveys and in the central regions of the fields of observations for numerous individual objects in the sky. In this case, the total area of all the observations with a depth better than 2.5×10^{-14} erg s^{-1} cm^{-2} performed by the NuSTAR telescope during its three-year stay in orbit does not exceed $\sim$0.5 deg^2 (Harrison et al. 2016). Thus, owing primarily to its wider field of view, the ART-XC telescope will be able to cover twice as much area with the same depth already in the first two weeks of observations.

The plans to use the main telescope of the SRG observatory, eROSITA, operating in the 0.2–10 keV energy band and having a wider field of view (1 deg in diameter) than ART-XC to conduct a deep ($\sim 5 \times 10^{-15}$ erg s^{-1} cm^{-2} in the 0.5–2 keV energy band) extragalactic survey with an area of $\sim$100 deg^2 during the SRG flight to the Lagrange point L2 (along with other observations to be performed at this testing stage of SRG operation) are being discussed at the moment. Conducting the hard X-ray ART-XC survey being discussed in this paper with an area of several deg^2 within a wider sky field that can be covered at lower energies by the eROSITA telescope is of natural interest. First, based on eROSITA data, it will be possible to measure the positions of most AGNs discovered by ART-XC much more accurately ($\sim 2'' - 3''$) and, thus, to facilitate their identification by a comparison with the available catalogs of sources and observations at ground-based telescopes. Second, based on the set of eROSITA and ART-XC data covering together a wide energy range, from $\sim$0.2 to $\sim$30 keV, it will be possible to find the candidates for Compton-thick AGNs with much greater confidence.

An improvement of the algorithm for the detection of sources based on ART-XT data aimed at a more optimal allowance for the spatial response of the X-ray optical system consisting of grazing-incidence mirrors and photodetectors is in our immediate plans. We expect that this will ultimately lead to a reduction in the effective size of the image spot in which a source is detected and, hence, to some lowering of the source confusion threshold. As a result, we are planning to work out more detailed recommendations regarding the depth and area of a possible ART-XC extragalactic survey.

ACKNOWLEDGMENTS

This work was supported in part by the Russian Foundation for Basic Research (project no. 16-29-13070-ofi-m). We are grateful to E.M. Churazov for the provided model spectra of AGNs.

REFERENCES

1. M. Ajello, J. Greiner, G. Sato, D. R. Willis, G. Kanbach, A. W. Strong, et al., Astrophys. J. **689**, 666 (2008).
2. D. M. Alexander, D. Stern, A. Del Moro, G. B. Lansbury, R. J. Assef, J. Aird, et al., Astrophys. J. **773**, 125 (2013).
3. M. Brightman and K. Nandra, Mon. Not. R. Astron. Soc. **413**, 1206 (2011).
4. R. A. Burenin, A. Vikhlinin, A. Hornstrup, H. Ebeling, H. Quintana, and A. Mescheryakov, Astrophys. J. Suppl. Ser. **172**, 561 (2007).
5. N. Cappelluti, M. Brusa, G. Hasinger, A. Comastri, G. Zamorani, A. Finoguenov, et al., Astron. Astrophys. **497**, 635 (2009).
6. R. della Ceca, T. Maccacaro, A. Caccianiga, P. Severgnini, V. Braito, X. Barcons, et al., Astron. Astrophys. **428**, 383 (2004).
7. E. Churazov, R. Sunyaev, M. Revnivtsev, S. Sazonov, S. Molkov, S. Grebenev, et al., Astron. Astrophys. **467**, 529 (2007).
8. E. Churazov, S. Sazonov, R. Sunyaev, and M. Revnivtsev, Mon. Not. R. Astron. Soc. **385**, 719 (2008).
9. M. Dadina, Astron. Astrophys. **485**, 417 (2008).
10. U. Feldman, Phys. Scr. **46**, 202 (1992).
11. R. Giacconi, A. Zirm, J. Wang, P. Rosati, M. Nonino, P. Tozzi, et al., Astrophys. J. Suppl. Ser. **139**, 369 (2002).
12. M. Gubarev, B. Ramsey, R. Elsner, S. O'Dell, J. Kolodziejczak, J. McCracken, et al., in *Space Telescopes and Instrumentation 2014: Ultraviolet to Gamma Ray,* Proc. SPIE **9144**, 91441V (2014).
13. F. A. Harrison, J. Aird, F. Civano, G. Lansbury, J. R. Mullaney, D. R. Ballantyne, et al., Astrophys. J. **831**, 185 (2016).
14. G. Hasinger, N. Cappelluti, H. Brunner, M. Brusa, A. Comastri, M. Elvis, et al., Astrophys. J. Suppl. Ser. **172**, 29 (2007).
15. R. Krivonos, A. Tkachenko, R. Burenin, E. Filippova, I. Lapshov, I. Mereminsky, et al., Exp. Astron. (2017, in press).
16. J. H. Krolik and M. C. Begelman, Astrophys. J. **329**, 702 (1988).
17. V. Levin, M. Pavlinsky, V. Akimov, M. Kuznetsova, A. Rotin, A. Krivchenko, et al., in *Space Telescopes and Instrumentation 2014: Ultraviolet to Gamma Ray,* Proc. SPIE **9144**, 914413 (2014).
18. V. Levin, M. Pavlinsky, V. Akimov, M. Kuznetsova, A. Rotin, A. Krivchenko, et al., in *Space Telescopes and Instrumentation 2016: Ultraviolet to Gamma Ray,* Proc. SPIE **9905**, 990551 (2016).
19. S. Lotti, C. Macculi, M. D'Andrea, L. Piro, S. Molendi, F. Gastaldello, et al., in *Space Telescopes and Instrumentation 2016: Ultraviolet to Gamma Ray,* Proc. SPIE **9905**, 990563 (2016).
20. B. Luo, W. N. Brandt, Y. Q. Xue, B. Lehmer, D. M. Alexander, F. E. Bauer, et al., Astrophys. J. Suppl. Ser. **228**, 2 (2017).
21. P. Magdziarz and A. A. Zdziarski, Mon. Not. R. Astron. Soc. **273**, 837 (1995).
22. A. Merloni, P. Predehl, W. Becker, H. Böhringer, T. Boller, H. Brunner, et al., arXiv e-prints (2012).
23. A. Moretti, C. Pagani, G. Cusumano, S. Campana, M. Perri, A. Abbey, et al., Astron. Astrophys. **493**, 501 (2009).
24. S. S. Murray, A. Kenter, W. R. Forman, C. Jones, P. J. Green, C. S. Kochanek, et al., Astrophys. J. Suppl. Ser. **161**, 1 (2005).
25. L. Nevot and P. Croce, Rev. Phys. Appl. **15**, 761 (1980).
26. M. Pavlinsky, V. Akimov, V. Levin, I. Lapshov, A. Tkachenko, N. Semena, et al., Proc. SPIE **8147**, 814706 (2011).
27. M. Pavlinsky, V. Akimov, V. Levin, A. Krivchenko, A. Rotin, M. Kuznetsova, et al., in *Space Telescopes and Instrumentation 2016: Ultraviolet to Gamma Ray,* Proc. SPIE **9905**, 99051J (2016).
28. P. Predehl, R. Andritschke, H. Böhringer, W. Bornemann, H. Bräuninger, H. Brunner, et al., in *Space Telescopes and Instrumentation 2010: Ultraviolet to Gamma Ray,* Proc. SPIE **7732**, 77320U (2010).
29. P. Ranalli, A. Comastri, C. Vignali, F. J. Carrera, N. Cappelluti, R. Gilli, et al., Astron. Astrophys. **555**, A42 (2013).
30. M. Revnivtsev, M. Gilfanov, R. Sunyaev, K. Jahoda, and C. Markwardt, Astron. Astrophys. **411**, 329 (2003).
31. S. Sazonov, R. Krivonos, M. Revnivtsev, E. Churazov, and R. Sunyaev, Astron. Astrophys. **482**, 517 (2008).
32. S. Sazonov, E. Churazov, and R. Krivonos, Mon. Not. R. Astron. Soc. **454**, 1202 (2015).
33. C. Tenzer, G. Warth, E. Kendziorra, and A. Santangelo, in *High Energy, Optical, and Infrared Detectors for Astronomy IV,* Proc. SPIE **7742**, 77420Y (2010).
34. Y. Ueda, M. Akiyama, G. Hasinger, T. Miyaji, and M. G. Watson, Astrophys. J. **786**, 104 (2014).
35. A. Vikhlinin, W. Forman, C. Jones, and S. Murray, Astrophys. J. **451**, 542 (1995).
36. A. Vikhlinin, B. R. McNamara, W. Forman, C. Jones, H. Quintana, and A. Hornstrup, Astrophys. J. **502**, 558 (1998).
37. D. C. Wells, E. W. Greisen, and R. H. Harten, Astron. Astrophys. Suppl. Ser. **44**, 363 (1981).

Translated by V. Astakhov